Hybrid Ray-Tracing-QuaDRiGa/FDTD for Realistic mmWave Exposure Assessment with Cell-Free MaMIMO in 3D Outdoor Environments

Robin Wydaeghe, Sergei Shikhantsov, Emmeric Tanghe, Günter Vermeeren, Luc Martens, Piet Demeester and Wout Joseph.

***Abstract*—Amid worry for 5G and 6G, the layman's question arises: "how much exposure do I *realistically* experience when I walk down the street?" Focusing on mmWave radio-frequency electromagnetic field exposure with Distributed Massive Multiple-Input Multiple-Output (DMaMIMO) technology, a new numerical method is proposed with a host of state-of-the-art (SOTA) advances to enable accurate exposure assessment anywhere on Earth. The new API for Google Earth 3D photorealistic tiles provides a high level-of-detail and high-coverage photogrammetry. We semantically classify the meshes with a SOTA deep learning model to distinguish classes such as buildings, terrain, and vegetation. Points along the path of a pedestrian are first ray-traced at 28 GHz millimeter waves with either a 6G DMaMIMO or realistically deployed 5G antenna systems as transmitter. The large-scale fading parameters are extracted and form the input for the QUAsi Deterministic RadIo channel GenerAtor (QuaDRiGa). QuaDRiGa then finely models the small-scale fading features of the channel along the full path with an omnidirectional User Equipment (UE) as receiver. The latter provides input for a hybridization procedure using a Huygens' box that models the EMFs around the UE. The new surface absorbed power density (S_{ab}) exposure metric is computed along the path using FDTD simulations of the MIDA anatomical phantom. A case study in Helsinki finds that the cell-free MaMIMO free-space exposure range is 20 dB more uniform than collocated MaMIMO. A case study in New York City finds that users experience on average a 20 dB higher values in exposure compared to non-users. The small-scale fading *hot-spot* phenomenon in realistic environments is studied in detail, showing on average a 12 dB electric field increase w.r.t. the background and a specific shape with up to 3 sidelobes, which is characterized quantitatively. The S_{ab} is less than 1% of the ICNIRP guidelines during all simulations at realistic Tx powers.**

5G, 6G, mmWave, RF-EMF, DMaMIMO, QuaDRiGa, FDTD, Ray Tracing, CF-MaMIMO, ICNIRP, Hot-spot, Exposure Assessment

I. Introduction

A. Scope

The fifth (5G) and sixth (6G) generation of cellular networks address the ever-increasing demands in internet connectivity [1]. They feature order of magnitude increases in antenna density and frequency, aiming to increase the spectral efficiency and data rates [2]. Infrastructure for the 5G sub-6 GHz bands is becoming widespread, with some cellular providers even deploying millimeter wave (mmWave) Base Stations (BSs) [3]. Among the enabling technologies are (1) Massive Multiple-Input Multiple-Output (MaMIMO), antennas composed of a large number of elements [4], and (2) the utilization of higher frequencies, such as mmWaves [5]. For the former, beamforming becomes possible by constructively interfering with each element's wavefront through phase and amplitude modulation. Beamforming actively concentrates the emitted radiation optimally toward the User Equipment (UE), in contrast with fourth-generation BSs which do not target active users. For the latter, higher bandwidths become available in unlicensed frequency bands, such as FR2, which operates around 26-28 GHz. However, these higher frequencies incur greater path loss. One proposed solution is 6G Distributed Massive Multiple-Input Multiple-Output (DMaMIMO) BSs [6]. Elements are distributed, e.g., on a building facade, reducing the path length to the UE. Cell-Free MaMIMO (CF-MaMIMO) is a prospective variant of this technology, where a very large number of synchronized Access Points (APs) are distributed throughout a large geographical area [7], [8]. Radio Stripes (RSs) are a prototype implementation of this paradigm [9].

A portion of the population is concerned that these new technologies could lead to adverse health effects, sparking deployment stops, protests, and general worry [10] [11]. Although deployed BSs always undergo stringent safety testing, research is needed to quantify the realistic Electromagnetic Fields (EMFs) from novel antenna systems in relation to the guidelines set by the International Commission on Non-Ionizing Radiation Protection (ICNIRP) [12]. A new surface-absorbed power density metric S_{ab} is introduced for frequencies above 6 GHz in the updated 2020 guidelines. Between the transmission of EMFs from the BS and the absorption in the human body, numerical dosimetry studies often focus on a specific part of the radio channel, making *worst-case* assumptions about other parts [13]. There is a gap in the current literature on *realistic* daily exposure from EMFs with comprehensive end-to-end simulations. The findings would interest both concerned citizens and policy-makers due to 5G and 6G's novelty. In addition, fully integrated simulations enable EMF-aware network planning. Here, the locations and powers of BSs in future networks can be realistically tuned before deployment. Finally, they enable the characterization of "hot-spots": wavelength-sized regions of increased EMF

All authors are with the Department of Information Technology, Ghent University/IMEC, 9052 Ghent, Belgium.
Corresponding author: Robin Wydaeghe (Robin.Wydaeghe@UGent.be).

shaped by the precoding of BS transmission, the propagation environment, and the user [14]–[16]. Besides some general features, the detailed characteristics of hot-spots in realistic environments are not known, especially at mmWave frequencies. Therefore, this work comprehensively studies hot-spots in realistic environments at 28 GHz.

To model the exposure from these technologies, the *propagation step* (computing the incident fields in an environment) needs to be interfaced with the *exposure step* (computing the absorbed exposure on a human) in one integrated method. The MaMIMO BS estimates the channel between receiver (Rx) and transmitter (Tx) using pilot waves. The transmitted symbols are then precoded in a process known as beamforming. For Line-Of-Sight (LOS) transmission scenarios, this causes (a) the direction of maximum gain to be aligned toward the Rx and (b) the individual elements' phases of the Tx to align causing constructive interference at the exact location of the UE's antenna [17]. When several beams impinge on the UE, either from multipath components or from a DMaMIMO system, a wavelength-sized region of increased EMF is formed at the location of the UE. Under Maximum Ratio Transmission (MRT) precoding, the Signal-to-Noise Ratio (SNR) at Rx increases without bounds as function of the number of antenna elements and channel diversity [4]. The maximum hot-spot E-field also increases with the received signal, but the relationship is unclear. The objective of this study is to study the effects of these hot-spots from MaMIMO BSs on human Radio-Frequency Electromagnetic Field (RF-EMF) exposure.

To inform the general public and policy-makers of realistic 5G EMF-levels, and to enable EMF-aware network planning, integrated end-to-end methods should be able to map exposure anywhere in the world. Google recently introduced an API for their photorealistic meshes [18]. The digital twin of the world provides environments with full 3D Level of Detail (LoD), instead of 2D or 2.5D LoD, required for accurate mmWave radio channel modeling [19], [20]. Conversely, the meshes are textured but not semantically labeled by Google. Recent advances in deep learning enable the semantic classification of these meshes to be performed with an accuracy of 93% [21].

Hybrid Ray Tracing (RT)/Finite-Difference Time-Domain (FDTD) is an example of an integrated method [22]. The method was used to study hot-spots at 3.5 GHz [14]. However, the first RT step is not appropriate to study exposure with high coverage in many different environments because RT is computationally intensive. Moreover, comprehensive data on the dielectric parameters and scattering of the materials is limited, especially at mmWave frequencies [23]. A new hybrid QUAsi Deterministic RadIo channel GenerAtor (QuaDRiGa)/FDTD method was proposed in [24] based on the state of the art (SOTA) QuaDRiGa [25]. QuaDRiGa renders the computations more efficient. However, the method is not suitable for site-specific simulations with high accuracy, as the Large-Scale Fading (LSF) does not align deterministically with the environment [15]. The computational requirements scale with the fourth power of frequency. Hence, there is a need to rethink the hybridization and exposure steps to obtain the exposure metrics efficiently.

B. Novelty

To the best knowledge of the authors, this work is novel in the following ways:

1) The first end-to-end method for exposure assessment at mmWaves. RT and QuaDRiGa simulations are leveraged efficiently, with a Huygens' box to interface the incident EMFs to FDTD simulations.
2) Premier application of high-accuracy high-coverage photogrammetry in a scientific publication, in particular to compute the realistic exposure along any path. For the first time, a semantic classifier is applied to these meshes.
3) Comparison of collocated and cell-free MaMIMO in both user and non-user scenarios at 28 GHz.
4) Characterization of realistic hot-spots at 28 GHz in realistic 3D environments. Their influence on the exposure metrics, the incident power density (S_{inc}) and new surface absorbed power density (S_{ab}) for frequencies above 6 GHz, is examined.

II. Methods

The integrated end-to-end method begins with a realistic walk of a user holding a smartphone and ends with the evaluation of the exposure metrics along this walk. The method chains 4 main steps in one pipeline. First, the configuration step, where the Rx, Tx, and environment are defined. Second, the propagation step, where the channel at the UE of the user is computed. Third, the hybridization step, where the EMFs impinging on the human body are computed. Fourth, the exposure step, where an FDTD and post-processing step returns the exposure metric. Fig. 1(a) illustrates the configuration and propagation steps, and Fig. 1(b) illustrates the configuration and propagation steps

A. Configuration step

A flowchart of the configuration step is detailed in Fig. 2.

1) Processed and classified environments: High-accuracy environments are essential for accurate ray-tracing simulations. In particular for mmWave frequencies, it is not sufficient to model building facades as flat surfaces [20] or street canyons without cars or lampposts [26]. Foliage is rarely modeled with individual trees. The wavelength at 28 GHz is 10.7 mm. Therefore, centimeter-sized features significantly affect the multipath diversity of the channel. A greater number of NLOS paths can be utilized to beamform the signal toward the UE. The API for photorealistic 3D tiles [18] is applicable to any location 3D-mapped by Google Earth. The reference in [27] provides the first examination of its accuracy compared to established methods.

The input for the entire pipeline follows from the origin and destination of the user's path. First, the quality of the mesh returned from the API is improved. Then, the mesh is split into 6 classes using a deep learning model [21]. Finally, the mesh is further simplified to be suitable for ray-tracing, and each class is assigned one suitable material.

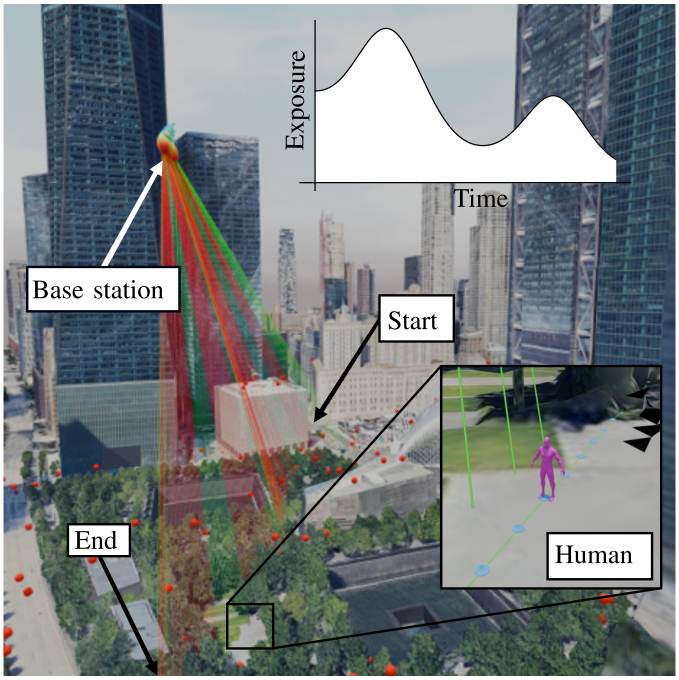

(a) A walk (blue dots) in the WTC of New York City (NYC) of a human (inset) is shown with the APs of a CF-MaMIMO system (red dots). The LOS/Non-Line-Of-Sight (NLOS) distinction from one specific AP is shown (green/red lines). A 3D realistic mesh from Google's 3D Tiles API [28] is retrieved to perform RT at 28 GHz on a coarse path.

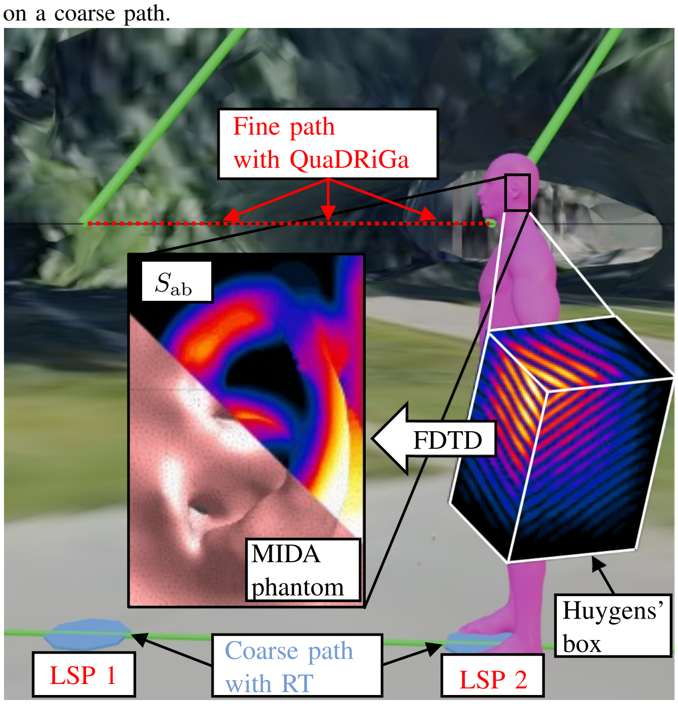

(b) A specific location is shown along the path. The blue dots denote the coarse points where RT is performed, from which LSPs are extracted. These form the input for the QuaDRiGa computations for the points in the fine path. The EMFs on a Huygens' are evaluated. These form the input for an FDTD simulation on the ear of the user, from which the S_{ab} exposure metric is extracted.

Fig. 1: Illustration of the (a) configuration and propagation steps, and the (b) hybridization and exposure steps.

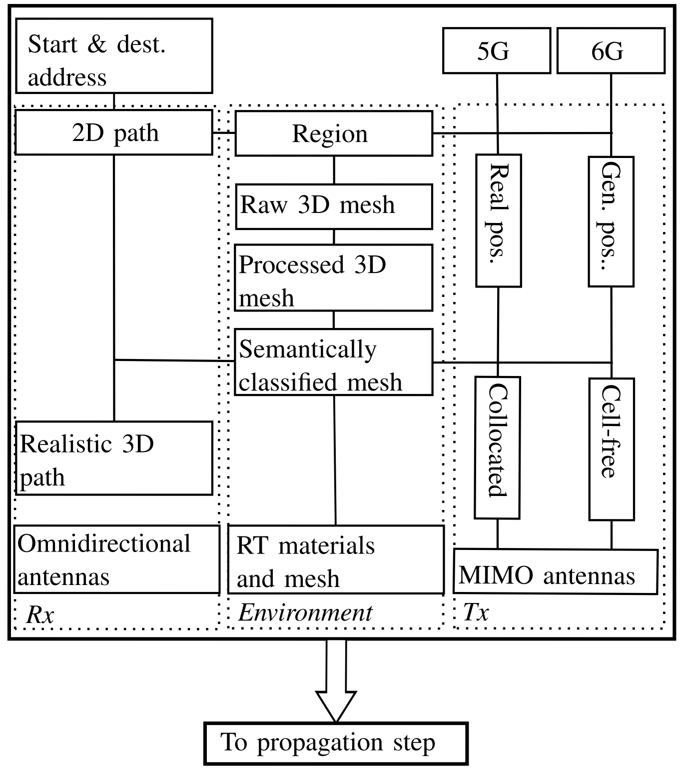

Fig. 2: Flowchart of the configuration step. The only input is the start and destination addresses that a pedestrian traverses. This outputs a 2D path and region around it. The 2D path is processed to a sampled set of 3D points along the path in the environment that are omnidirectional antennas, representing the Rx. The region defines the environment, which is processed for use in RT simulations. The region also defines the locations of MIMO BSs, either collocated when studying 5G or cell-free when studying 6G.

2) Receiver path: The channel and exposure are computed along a path a user takes. The user's path is composed of series of waypoints forming the fastest path between the origin and destination addresses, as determined by the Google Maps Directions API [29]. These waypoints are then subsampled linearly. The Google API causes the user to walk realistic paths, as the waypoints are on walkable routes, such as sidewalks. To eliminate discontinuous changes in direction of travel, the user is modeled to always walk toward the point that is 2 m ahead on the straight path, subsampling the path every wavelength. The final path can clip with the environment, in which case the points are discarded. The elevation of the points follows the terrain. 1.5 m is added to this elevation to take the average height of the UE into account. The user walks at a constant speed of 1.4 m/s. Each point along the path is timestamped in order to average fields along time.

3) Antenna locations in a 5G network: The realistic locations of 5G BSs are not available on a global scale. One possible solution is open services that aggregate BS locations based on GPS location and signal strength through crowd-sourcing. For this work, the OpenCellID API [30] provides the location of real cellular BSs with high coverage. Locations are determined using crowd-sourced data. Therefore, the accuracy depends on the number of measurements and the propagation model used to triangulate BSs positions. Only the antenna density is representative of the physical twin. This is illustrated in Fig. 1(a) with red dots.

4) Antenna locations in a 6G network: A 6G CF-MaMIMO Access Point Network (APN) is a system that comprises a very large number of distributed APs which simultaneously serve a much smaller number of users over a wide area [7], [8]. Here, APs are placed on the facades of buildings. First, building mesh faces whose normal have an azimuthal angle between 70 and 90 degrees and with heights 3 meters above the ground, are selected. Then, uniform Poisson disc sampling with a minimum distance of 10 m is performed using the efficient Bridson's algorithm [31]. 1.5 m above the nearest ground mesh, vertically-polarized omnidirectional antennas model the UE (e.g. a smartphone) being held by the pedestrian.

B. Propagation step

A flowchart of the propagation step is detailed in Fig. 3. From the configuration step, the Rxs along the path, the environment and the Tx's antenna elements are loaded in. This forms the input for RT simulations evaluated for all Rxs and Txs for every 1 m along the path. The output is the LSF channel and the 7 Large-Scale Parameters (LSPs) for each point along the coarse path. Using QuaDRiGa, the path is split into segments. Within each segment, the LSPs are statistically aggregated to form the input for the QuaDRiGa computation along the fine path. The output is the SSF channel and the Last-Bounce-Scatterers (LBSs). In a post-processing step, the former is combined with the LSF channel to obtain the *multi-path matrix*, with entries for 4 dimensions: receivers i, antenna elements j, LBSs l and distance snapshots s. Precoding is applied to the transmitted symbols. A *precoded multipath matrix* and the LBSs form the input for the hybridization step.

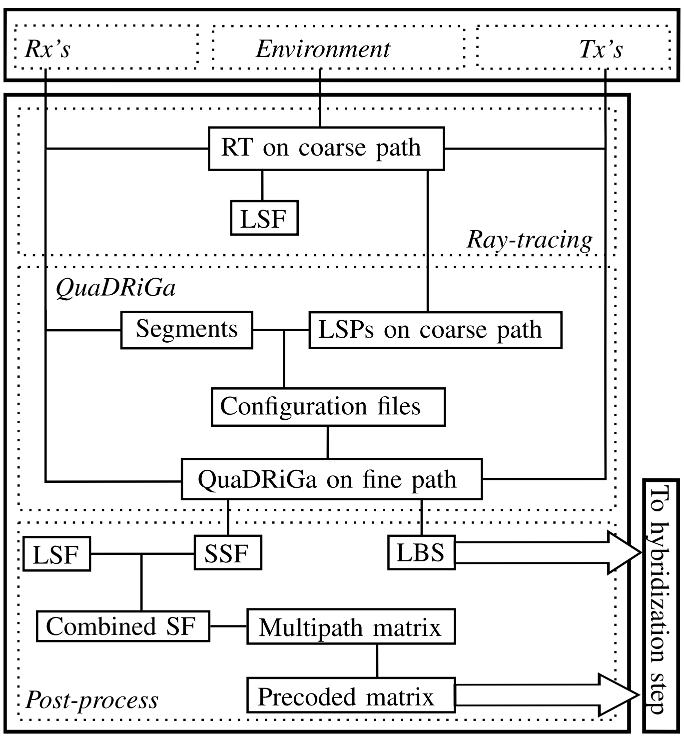

Fig. 3: Flowchart of the propagation step. The upper box refers to the output of the configuration step in Fig. 2. In the central box, the propagation step combines RT and QuaDRiGa simulations for the LSF and Small-Scale Fading (SSF) modelling of the channel, respectively. These are post-processed and form the input for the hybridization step shown on the bottom right (Fig. 4).

The propagation step involves simulating the wireless channel based on the configuration, defining all Txs, Rxs and the 3D environment between them. Channel models can be broadly classified into deterministic and stochastic models. Based on the survey in [32], the SOTA among these channel models are selected.

1) Ray-tracing: RT is a deterministic channel model. In Shooting and Bouncing Rays (SBR) RT, rays shoot out from the Txs, propagate and scatter through the environment, and are collected at the Rxs. The advantage of RT is its potential to exactly model the underlying electromagnetic field problem in the high frequency limit, especially suitable for 5G and 6G mmWave channel models. Therefore, RT enables site-specific simulations that can match the corresponding measurements [33]. An important disadvantage of the method is the need for an accurate description of EMF scattering properties for different materials in the scene [23]. The data on this remain sparse in the literature. Moreover, the LoD for the meshes must be in the order of the wavelength [20]. This requires a fine semantically classified environment at mmWaves frequencies. All these factors cause the accuracy of the Channel Impulse Response (CIR) to be insufficient for large scale RT simulations. RT is also more computationally demanding compared to stochastic or map-based channel models. Derived parameters such as the LSPs and their correlation matrix agree more robustly with measurements than the CIR. RT simulations are done every meter along the path.

The commercial solver Wireless Insite [34] is employed to perform the RT simulations. The Tx, Rx, and semantically classified environments are imported into the software. The six classes of materials are assigned the constitutive parameters shown in Table I. The SBR method is employed with 5 reflections, 1 diffraction, and 0 transmissions. The maximum angular separation between rays at the transmitter is 0.25°. The radius of the collection sphere at the receiver is 20 cm. Diffuse scattering was not modeled. For each combination of i, j and s, $N^{\text{rays}}_{i,j,s}$ rays are retained if their power is at least -250 dBm at the receiver. The result is cast in a *multipath matrix* $\mathbf{M}^{\text{RT}}$ with dimensions $N \times M \times \left(\max N^{\text{rays}}_{i,j,s}\right) \times N^{\text{RT}}_{\text{snapshot}}$.

2) QuaDRiGa: The QuaDRiGa tool is used to generate realistic quasi-deterministic impulse responses from each AP to each receiver over time. QuaDRiGa is a quasi-deterministic channel model, but is classified as Geometry-based Stochastic Channel Model (GSCM) with a large number of features [32]. Configuration files containing the stochastic information from measurement campaigns in LOS/NLOS urban/suburban environments are available in the software. Based on these, a spatially-consistent stochastic parameter map of the LSPs is

TABLE I: Constitutive Parameters for Different Classes of Materials in Ray Tracing at 28 GHz [35] [36]. Note that vegetation is not modeled as a stochastic scatterer.

Material Class	Relative permittivity ϵ_r	Conductivity σ (S/m)
Buildings (concrete)	5.24	0.6260
Terrain (asphalt)	5.7	$5 \cdot 10^{-4}$
High Vegetation	10	0.1
Cars	PEC[a]	PEC
Water	80	4
Boat	PEC	PEC

[a]Perfect Electric Conductor

generated within each channel scenario [25]. Within segments along the path, stationary scattering clusters are generated around the receiver with properties that correspond to the parameter map. With the positions of the clusters known, a deterministic channel is obtained along the path of a moving user. This open-source model and its previous iterations have been validated for over two decades and comply with the 3GPP guidelines [37]. This tool was chosen as a component of our numerical pipeline for three reasons. First, QuaDRiGa provides realistic channels because the statistical parameters that generate parameter maps are derived from measurement campaigns [25], [38]. In addition, version 2.0 features spatial consistency in the channels, which is important when modeling the resulting exposure along a path [39], [40]. Finally, the channel generator is computationally more efficient than deterministic methods to model the large number of channels in CF-MaMIMO scenarios.

A number of LBS clusters, each with a number of subclusters, are generated around the user. The birth and death of clusters together with interpolations of their positions and powers also assure spatial consistency in the transitions between channel scenarios. Therefore, the hot-spot shape and exposure metrics consistently conform to the path and environment variations. Computing the fields emitted from each subcluster is too computationally expensive. Instead, at most $N_{i,j,s}^{\text{subclusters}}$ beams with the greatest power are selected for a combined channel. $N_{i,j,s}^{\text{subclusters}}$ is chosen such that 99% of the power is accounted for in selected subclusters. Unselected subclusters have their total power (1%) spread uniformly over the selected ones. Multi-user scenarios can be implemented by defining an origin and destination address for each receiver and repeating the above steps. The QuaDRiGa software is modified to yield a multipath matrix $\mathbf{M}^{\text{QD}}$ with dimensions $N \times M \times \left(\max N_{i,j,s}^{\text{subclusters}}\right) \times N_{\text{snapshot}}^{\text{QD}}$, and the positions of the subclusters at each snapshot.

Hybrid QuaDRiGa/FDTD that is not based on RT uses the configuration files of the mmMAGIC model, valid for frequencies above 6 GHz, a UE height of 1.5 meters and a Tx height of 6 to 10 meters [41]. For each point in the path, we manually assign a channel scenario based on the type of environment, e.g., dense urban, suburban, or rural. For each Tx, if the LOS connection is obstructed, the channel scenario is classified as NLOS and vice versa.

3) Ray-tracing based QuaDRiGa: Hybrid RT/FDTD was used for the first time at mmWaves in [22]. This enabled a realistic, site-specific evaluation of the exposure metrics on humans in a factory-of-the-future. Hybrid RT/FDTD is computationally challenging because the full EMFs for many Direction of Arrivals (DoAs) need to be loaded to memory [42]. This was alleviated by introducing a Huygens' box as interface and applied to a small region in NYC in [15]. Despite improvements in efficiency, RT remains computationally demanding for environments larger than 100 m^2.

QuaDRiGa was hybridized for the first time with the FDTD method in [24]. The propagation step could then be computed faster and with more APs than with hybrid RT/FDTD. This enables the computation of exposure on the city scale, with an order of magnitude more APs and users. However, results can only be interpreted statistically over a large number of samples. Due to the stochastic nature of GSCMs, the site-specific geometry is lost with the exception of environment classification into LOS/NLOS and urban/sub-urban/rural.

This paper introduces for the first time a new hybrid propagation model: *RT-based QuaDRiGa*. Falling under the map-based deterministic channel classification [32], this model represents the SOTA in the wireless channel modeling literature by combining the benefits of both deterministic and stochastic models. Previous research has focused on substituting RT with QuaDRiGa using appropriate LSPs [43]. This work presents a method to retain the physical accuracy of RT while leveraging the speed of QuaDRiGa. Points ever 1 meter along the path of each user are chosen to evaluate the LSF variations in the environment. RT simulations compute the 8 LSPs for these points:

1) Root-Mean-Squared delay spread
2) Ricean K-factor
3) Shadow fading
4) Azimuth spread of departure
5) Azimuth spread of arrival
6) Elevation spread of departure
7) Elevation spread of arrival
8) Cross-polarization ratio

QuaDRiGa splits the path for each receiver in segments. The length of segments is drawn from a normal distribution with a mean of 40 m, a standard deviation of 5 m, and minimum/maximum of 30/70 m, respectively. A new segment is also created when the receiver transitions between the LOS and NLOS states. Within these segments, the 7 LSPs (shadow fading is not considered) are aggregated statistically by computing the log-normal mean, standard deviation, decorrelation distances and inter-parameter correlation matrices. These form the stochastic basis for the QuaDRiGa method. The data is collected in configuration files. These are generally used to characterize different radio environments classified by urbanicity. Then, QuaDRiGa computes the channel along the full path, capturing the SSF variations. For each Rx/Tx link, the LSF and SSF parts are combined.

In the following, we construct the combined multipath matrix $\mathbf{M} \in \mathbb{C}^{N \times M \times L \times S}$ with $L = \max N_{i,j,s}^{\text{subclusters}}$ and $S = N_{\text{snapshot}}^{\text{QD}}$. In general, the corresponding channel matrix $\mathbf{H}_s$ for snapshot s is the sum over either all subclusters in QuaDRiGa or all collected rays in RT in a link between receiver i and transmitter j:

$$\mathbf{H} = \sum_l \mathbf{M}_l \,. \tag{1}$$

Consider a segment along the walk starting and ending at a distance a and b, respectively. $\mathbf{H}_s^{\mathrm{QD}}$ are the channels obtained from QuaDRiGa simulations on distances $s\delta d$. $\mathbf{H}_n^{\mathrm{RT}}$ are the channels obtained from ray-tracing simulations on distances $n\Delta d = n(q\delta d)$, with $q = N_{\mathrm{snapshot}}^{\mathrm{QD}}/N_{\mathrm{snapshot}}^{\mathrm{RT}} \gg 1$. First, $\mathbf{H}^{\mathrm{QD}}$ is adjusted such that its start and end values align with $\mathbf{H}^{\mathrm{RT}}$ within the segment:

$$\widehat{\mathbf{H}}_s^{\mathrm{QD}} = \mathbf{H}_s^{\mathrm{QD}} + \frac{s\delta d - a}{b-a}\left(\mathbf{H}_{b/\Delta d}^{\mathrm{RT}} - \mathbf{H}_{b/\delta s}^{\mathrm{QD}}\right) - \frac{s\delta d - b}{b-a}\left(\mathbf{H}_{a/\Delta d}^{\mathrm{RT}} - \mathbf{H}_{a/\delta d}^{\mathrm{QD}}\right)\,,\ \forall\, a \le s\delta d \le b\,.$$

This is repeated for all segments in the path. Second, the moving average of this adjusted function is subtracted from itself:

$$\widetilde{\mathbf{H}}_s^{\mathrm{QD}} = \widehat{\mathbf{H}}_s^{\mathrm{QD}} - \frac{1}{2u}\sum_{s'=s-u}^{s+u} \widehat{\mathbf{H}}_{s'}^{\mathrm{QD}}\,,\ \forall\, u \le s \le S-u\,,$$

where u is chosen here to be half of the RT steps, $q/2$. The resulting $\widetilde{\mathbf{H}}$ captures the SSF variations. Finally, a RT-based QuaDRiGa function $\mathbf{H}^{\mathrm{RT/QD}}$ is obtained by adding these SSF variations to the linear interpolation of $\mathbf{H}^{\mathrm{RT}}$ on the finer multiples of δd:

$$\mathbf{H}_s^{\mathrm{RT/QD}} = \mathbf{H}_{s,\mathrm{interp}}^{\mathrm{RT}} + \widetilde{\mathbf{H}}_s^{\mathrm{QD}}\,.$$

The combined multipath matrix is obtained by:

$$\mathbf{M}_l = \mathbf{M}_l^{\mathrm{QD}} \odot |\mathbf{H}^{\mathrm{RT/QD}}| \oslash |\mathbf{H}^{\mathrm{QD}}|\,, \tag{2}$$

where $\odot$ and $\oslash$ are the Hadamard element-wise multiplication and division operators. Using this rescaling, the more accurate amplitude information from RT is used, but the precise phase information from QuaDRiGa is retained.

4) Precoding: When computing the downlink exposure from a CF-MaMIMO 6G system, [24] assumed that every AP holds one antenna. However, these systems integrate multiple antenna elements within each AP. This is the case, e.g., in RSs. Due to the small wavelength at 60 GHz, up to sixteen elements fit within the thin stripes. This paper presents results for a large number of APs of 4×4 patch antennas, distributed in the environment. We consider a noiseless channel where each antenna element radiates with phases and amplitudes $\boldsymbol{x} \in \mathbb{C}^{M\times1}$ and each UE receives a signal $\boldsymbol{y} \in \mathbb{C}^{N\times1}$

$$\boldsymbol{y} = \mathbf{H}\boldsymbol{x}\,.$$

As precoding is performed similarly for each snapshot s, this index is omitted for clarity. Precoding is performed with MRT normalized to a power P using vector normalization. The precoding matrix $\mathbf{W}$ is [44]

$$\mathbf{W} = \sqrt{\frac{P}{N}}\left[\frac{\mathbf{f}_1}{\|\mathbf{f}_1\|} \cdots \frac{\mathbf{f}_N}{\|\mathbf{f}_N\|}\right]\,, \tag{3}$$

where $\mathbf{f}_i$ are column vectors of the hermitian conjugate of the channel. As the antenna elements within one AP cannot cooperate with antenna elements from other APs, the precoding is performed in two steps.

In the first step, the powers and phases of each elements in the 4×4 arrays are tuned to beamform toward the user. For an AP $J = 1,\ldots,\mathcal{M}$ that contains the antenna elements j with indices $\mathcal{J}(J)$, the entries of its associated precoding matrix are

$$w_{j,i}^J = \begin{cases} \dfrac{h_{i,j}^*}{\sqrt{N\sum_j |h_{i,j}|^2}} & \forall\, j \in \mathcal{J}(J) \\ 0 & \forall\, j \notin \mathcal{J}(J) \end{cases}\,, \tag{4}$$

where $P = 1\,\mathrm{W}$. The phases and amplitudes of the antenna elements are independently added for each AP

$$\widehat{\boldsymbol{x}} = \sum_J \widehat{\boldsymbol{x}}^J = \sum_J \sum_i \mathbf{w}_i^J s_i\,,$$

where $\boldsymbol{s} \in \mathbb{C}^{N\times1}$ is the transmitted symbol. However, the phases and amplitudes are not final, as denoted by a hat, because there is no coordination between the APs yet. The received signal from AP J is

$$\widehat{\boldsymbol{y}}^J = \mathbf{H}\widehat{\boldsymbol{x}}^J\,,$$

or for each subcluster

$$\widehat{\boldsymbol{y}}_l^J = \mathbf{M}\widehat{\boldsymbol{x}}^J\,.$$

We can now define an intermediary multipath matrix $\widehat{\mathbf{M}} \in \mathbb{C}^{N\times\mathcal{M}\times L\times S}$ which embeds these phases and amplitudes in its matrix elements:

$$\widehat{M}_{i,J,l,s} = \widehat{y}_{i,J,l,s}\,.$$

In the second step, the phases and amplitudes of APs as a whole are tuned to beamform toward the user. The precoding matrix $\mathbf{W}$ of the entire APN is defined as in (3) but with

$$\mathbf{F} = \widehat{\mathbf{H}}^H\,, \tag{5}$$

where $\widehat{H}$ is the intermediary channel computed with (1). All exposure results are linear w.r.t. to the total power P allotted to the network in (3). The final phases and amplitudes of all antenna elements in the APN are

$$\boldsymbol{x} = \sum_i \mathbf{w}_i s_i\,.$$

The final *precoded multipath matrix* similarly embeds the transmitters' phases and amplitudes with symbol $\boldsymbol{s}$ such that its entries are the received signal at the UEs:

$$m_{i,j,l,s}^{\mathrm{precoded}} = \hat{m}_{i,j,l,s}\cdot x_{j,s}\,.$$

The precoded case will be compared with the *unprecoded* case. Here, $h_{i,j}$ and $f_{i,j}$ in (4) and (5) are set to $\exp j\phi_{i,j}$ where $\phi_{i,j}$ are random numbers between $[0,2\pi)$. As the precoding acts on a completely different channel, the phases and amplitudes $x^{\mathrm{unprecoded}}$ will no longer cause beamforming toward the user. The final unprecoded multipath matrix is

$$m_{i,j,l,s}^{\mathrm{unprecoded}} = \hat{m}_{i,j,l,s}\cdot x_{j,s}^{\mathrm{unprecoded}}\,,$$

where $x_{j,s}^{\mathrm{unprecoded}}$ arises from a normalized precoding matrix. MRT precoding cannot place a null on a non-user. A non-user can however experience increased exposure when entering the LSF hot-spot from an active user. Hence, the case of unprecoded transmission, where beamforming is disabled, is comparable to a non-user scenario when aggregated over many samples.

C. Hybridization step

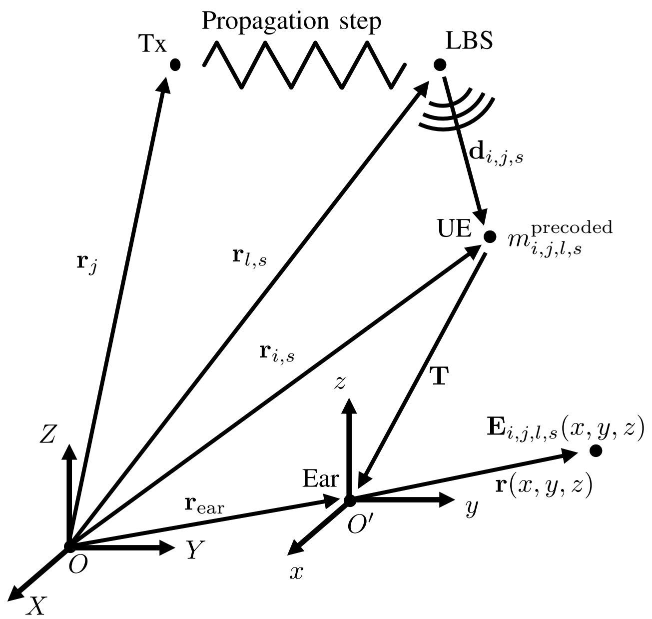

Fig. 4: Overview of vectors related to the hybridization step. A global coordinate system O defines the positions of an antenna element j in a MIMO BS (Tx), a QuaDRiGa LBS l at time-snapshot s, the antenna of the UE held by user i at time snapshot s, and center of the evaluated exposure region (Ear) at time snapshot s. This center defines a new moving coordinate system O', parallel to O and translated by $\mathbf{r}_{\text{ear}}$. The final electric field $E_{i,j,l,s}(x,y,z)$ is defined in O' and emanates from the LBS (one of the scatterers in a QuaDRiGa cluster).

The geometry of the hybridization step is shown in Fig. 4. The indices i, j, l, s form a combination of Rx, Tx (element), subcluster LBS and distance snapshot, respectively, for which the electric field is computed. The Huygens' box function within the numerical pipeline is illustrated in Fig. 1(b). A Huygens' surface is used as interface with the exposure step, requiring saving the fields only on the surface of the box [45].

First, we describe the approach in free space. Section II-D will consider the case where the channel is altered because the impinging fields are scattered by the anatomical phantom. For a vertically-polarized omnidirectional receiving antenna, the channel in (2) can be related to the electric field at the UE.

$$m^{\text{precoded}}_{i,j,l,s} = \frac{1}{A_F}\mathbf{E}_{i,j,l,s}(-\mathbf{T})\cdot\mathbf{e}_\theta(\theta_{i,l,s},\phi_{i,l,s}) \;, \qquad (6)$$

where A_F is the antenna factor in m^{-1} of the omnidirectional antenna, θ and ϕ angles are the spherical coordinates of the impinging electric field $\mathbf{E}_{i,j,l,s}$ on the UE and $\mathbf{e}_\theta$ is the unit vector along θ. This expression holds true at the antenna of the UE. The total fields are now computed on the bounding box around the location of the user's right ear. Their coordinates $\mathbf{r}(x,y,z)$ are with respect to a new origin O' at $\mathbf{r}_{\text{ear}} = \mathbf{T}+\mathbf{r}_i$, where $\mathbf{T}$ is the translation between the UE's antenna and the ear. In O', the electric field's spatial component ξ in the far-field from a subcluster to $\mathbf{r}(x,y,z)$ behaves as

$$\xi(x,y,z) = A\frac{\exp\left(jk\left|\mathbf{d}_{i,l,s}+\mathbf{T}+\mathbf{r}(x,y,z)\right|\right)}{\left|\mathbf{d}_{i,l,s}+\mathbf{T}+\mathbf{r}(x,y,z)\right|} \;, \qquad (7)$$

where $\mathbf{d}_{i,l,s} = \mathbf{r}_{i,s} - \mathbf{r}_{l,s}$ and A is its amplitude, normalized to unity at the UE

$$A = \exp\left(-jk\left|\mathbf{d}_{i,l,s}\right|\right)\left|\mathbf{d}_{i,l,s}\right| \;.$$

An expression can be constructed for the electric field around the UE:

$$\mathbf{E}_{i,j,l,s}(x,y,z) = A_F m^{\text{precoded}}_{i,j,l,s}\xi(x,y,z)\mathbf{e}_\theta(\theta_{i,l,s},\phi_{i,l,s}) \;. \qquad (8)$$

By summing over all Txs and subclusters, the total EMFs are obtained

$$\mathbf{E}_{i,s} = \sum_{j,l}\mathbf{E}_{i,j,l,s} \;,$$

$$\mathbf{H}_{i,s} = \sum_{j,l}\frac{1}{Z_0}\frac{\mathbf{d}_{i,l,s}}{\left|\mathbf{d}_{i,l,s}\right|}\times\mathbf{E}_{i,j,l,s} \;.$$

These fields are evaluated on the sides of the Huygens' box on the same Yee-grid as the FDTD simulation. Hence, the computational and memory requirements scale quadratically with frequency instead of cubically.

D. Exposure step

1) User-induced coupling of the channel: The function of the exposure simulation within the numerical pipeline is illustrated in Fig. 1(b). MRT precoding of the symbols causes the transmitted beam's direction of maximal gain to be aligned toward $\mathbf{r}_{i,s}$, in particular for LOS and collocated antennas [42]. This is a *large-scale hot-spot*, which can induce higher fields to nearby non-users. In addition, alignment of the amplitudes and phases from different beams causes an additional hot-spot gain at $\mathbf{r}_{i,s}$ if $\mathbf{r} = -\mathbf{T}$. This is the *small-scale hot-spot* and is studied in detail in this work. As reference quantities are determined in free-space receiving scenarios, the time-averaged incoming power density S_{inc} is readily available. However, to compute the basic quantities, an anatomical phantom is included in the FDTD simulations, which invalidates (6) and eliminates the small-scale hot-spot effect. This user-induced coupling is included here based on [46], but with the rays substituted by QuaDRiGa subclusters. We opted to use a simple vertical electric edge source at 28 GHz, placed 1 cm orthogonally to the median plane from the tip of the right ear. A voltage of 1 V over the terminals is simulated using FDTD with the anatomical phantom. Based on [46], the reciprocity between transmitting and receiving [47] can be leveraged to compute the antenna pattern $A(\theta,\phi)$ directly using the far-field pattern of any UE antenna. However, this only holds for impinging plane waves, i.e., when the clusters are infinitely far. To prove this, consider a set of angles (θ_p,ϕ_p). For each, a cluster p is placed infinitely far with this orientation from the user in O'. Therefore, spherical wavefronts are neglected in the user-induced coupling. An impinging electric field from this cluster is defined such that the channel (6) equals 1 V at the UE in free space (fs):

$$1 = \frac{1}{A_F} \mathbf{E}_p^{\text{fs}} \left(-\mathbf{T}\right) \cdot \mathbf{e}_\theta \left(\theta_p, \phi_p\right) \ .$$

Therefore, $\mathbf{E}_p^{\text{fs}}$ is a plane wave with an amplitude of A_F and direction (θ_p, ϕ_p). By setting $\mathbf{E}_p^{\text{fs}}(x, y, z)$ as source on the Huygens' box, an FDTD simulation is performed and the voltage V over the UE's antenna terminal is measured

$$A^\theta(\theta_p, \phi_p) \triangleq V\left(\mathbf{E}_p^{\text{scattered}}\left(-\mathbf{T}\right)\right) \ . \tag{9}$$

The $\mathbf{E}_p^{\text{fs}}$ field is scattered by the presence of the anatomical phantom to produce $\mathbf{E}_p^{\text{scattered}}$ at the UE. Using this method, a vertically polarized antenna pattern $A^\theta(\theta, \phi)$ is retrieved. The uncoupled channel in free space can now be extended by this antenna pattern to obtain the coupled channel:

$$c_{i,j,l,s}^{\text{coupled}} = A^\theta(\theta_{i,l,s}, \phi_{i,l,s}) c_{i,j,l,s}^{\text{uncoupled}} \ ,$$

where $c_{i,j,l,s}^{\text{uncoupled}}$ refers to the channel in (2). Therefore, the precoding process should be executed only after this modification. When $\theta_{i,l,s}$ or $\phi_{i,l,s}$ does not correspond to one of the discrete angles (θ_p, ϕ_p), a bilinear interpolation is performed to estimate the antenna pattern. As the antenna pattern $A(\theta, \phi)$ needs to only be computed once for a specific exposure setup, this can be done as a preprocessing step.

2) FDTD simulations: The surface currents from the Huygens' box form generalized total-field scattered-field sources in an FDTD simulation that includes the Multimodal Imaging-Based Detailed Anatomical Model of the Human Head and Neck (MIDA) [48] as virtual phantom, featuring a spatial isotropic resolution of 500 µm. The surface needs to be gridded with a resolution of at least 10 cells per wavelength. The head is not oriented along the user's path. In FDTD simulations, the number of unknowns scale as f^3 and the simulation time as f [42]. However, all impulse responses for each DoA do not need to be kept in memory as in [22]. mmWave 5G and 6G operate at frequencies above 6 GHz, e.g. 28 GHz. The maximum time-averaged S_{ab} (in W/m^2) on a 4-cm^2 surface is used to better account for the superficial nature of the exposure [12]. At 28 GHz, the penetration depth is approximately 0.92 mm $\approx \lambda/10$ [12], such that the field distribution cannot be resolved efficiently in FDTD. Therefore, a SOTA coated dielectric skin model is used on a homogeneous phantom [49], [50]. This exposure quantity is computed in a post-processing step with the skin of the virtual phantom [51].

3) Hot-spot characterization: In [15], the shape of a hot-spot was studied in an experimental setup. The hot-spot features a large-scale hot-spot around the receiver, a small-scale hot-spot as a result of the interference pattern, prominent sidelobes and spherical wavefronts. Similar results are seen at 3.5 GHz [14]. The aforementioned study validated the hybridization part of our tool because the experiment matched the simulation well.

Two methods to define the location of hot-spots are examined. First, exactly where the UE is located and second, where the fields are highest in a small region around the UE. At this location, three slices are taken normal to the x-, y- and z-planes. A peak-finding algorithm detects whether a hot-spot is present along each axis. We introduce three properties to characterize the hot-spots:

1) The *dimensionality* of a hot-spot is the number of axes where a hot-spot was found.
2) The Full Width at Half Maximum (FWHM) is the average of all detected FWHMs.
3) The Prominence-to-Peak (P/P) ratio provides a representation of the hot-spot's dynamic range, where a ratio of 1 is a peak flanked by fields equaling 0.

Two methods are proposed to average exposure metrics over time. In the first method, the exposure metrics S_{inc} and S_{ab} are considered for each time step in the walk. The average exposure metrics are then the average of all these over time. This is coined *exposure-wise* averaging, because the concept of "exposure at each time step" is correctly interpreted. These values correspond to the ICNIRP time-averaged exposure metrics for intervals of 6 minutes. In the second method, the average of the electric and magnetic fields over time is considered first. The average exposure metrics S_{inc} and S_{ab} are then computed for these average EMFs. This is coined *propagation-wise* averaging, because the concept of "average propagated EMFs" is correctly interpreted. These values provide insights into how interference typically forms the shape of a hot-spot. Thus, the equations for incident power density are the following:

$$\begin{aligned} S_{\text{inc,exposure-wise}}(\mathbf{r}) &= \langle |\mathbf{E}(\mathbf{r}) \times \mathbf{H}(\mathbf{r})| \rangle \ , \\ S_{\text{inc,propagation-wise}}(\mathbf{r}) &= |\langle \mathbf{E}(\mathbf{r}) \rangle \times \langle \mathbf{H}(\mathbf{r}) \rangle| \ , \end{aligned} \tag{10}$$

where $\langle \cdot \rangle$ is the average of a quantity with respect to time. Analogous formulas apply for S_{ab}.

III. RESULTS

A. Case study in Helsinki, Finland

In this case study, hybrid QuaDRiGa/FDTD is applied to a single-user scenario of a 6G cell-free massive MIMO network and compared with a 5G collocated MIMO antenna. Fig. 5 shows the configuration of this case study. The signals are precoded toward a smartphone held in the hand of a pedestrian. The user walks the blue path shown in the inset of Fig. 5, near St. John's Church in Helsinki. The total distance of the walk is 273 m. The pedestrian is in an urban environment in the first and last 50 m. In between, the user walks through the park of St. John's church in central Helsinki. Due to the increased vegetation and absence of buildings, the environment in this section is suburban. A collocated 8×8 MIMO antenna is placed on the tower of the church, facing south and tilted down by 15°.

The hybrid QuaDRiGa/FDTD method is applied with a carrier frequency of 28 GHz. The sampling rate is 53 Hz (such that there are 2.46 wavelengths between each snapshot) and the total number of distance snapshots (or evaluation points) is 9905. 335 distributed APs were generated in the $250\,\text{m} \times 250\,\text{m}$ area around the path. The FDTD grid and Huygens' surface have a resolution of 15 cells per wavelength resulting in a grid of $302 \times 230 \times 323$ cells. The average computation time for one snapshot of hybrid QuaDRiGa/FDTD is 160 sec. In this case study, we choose

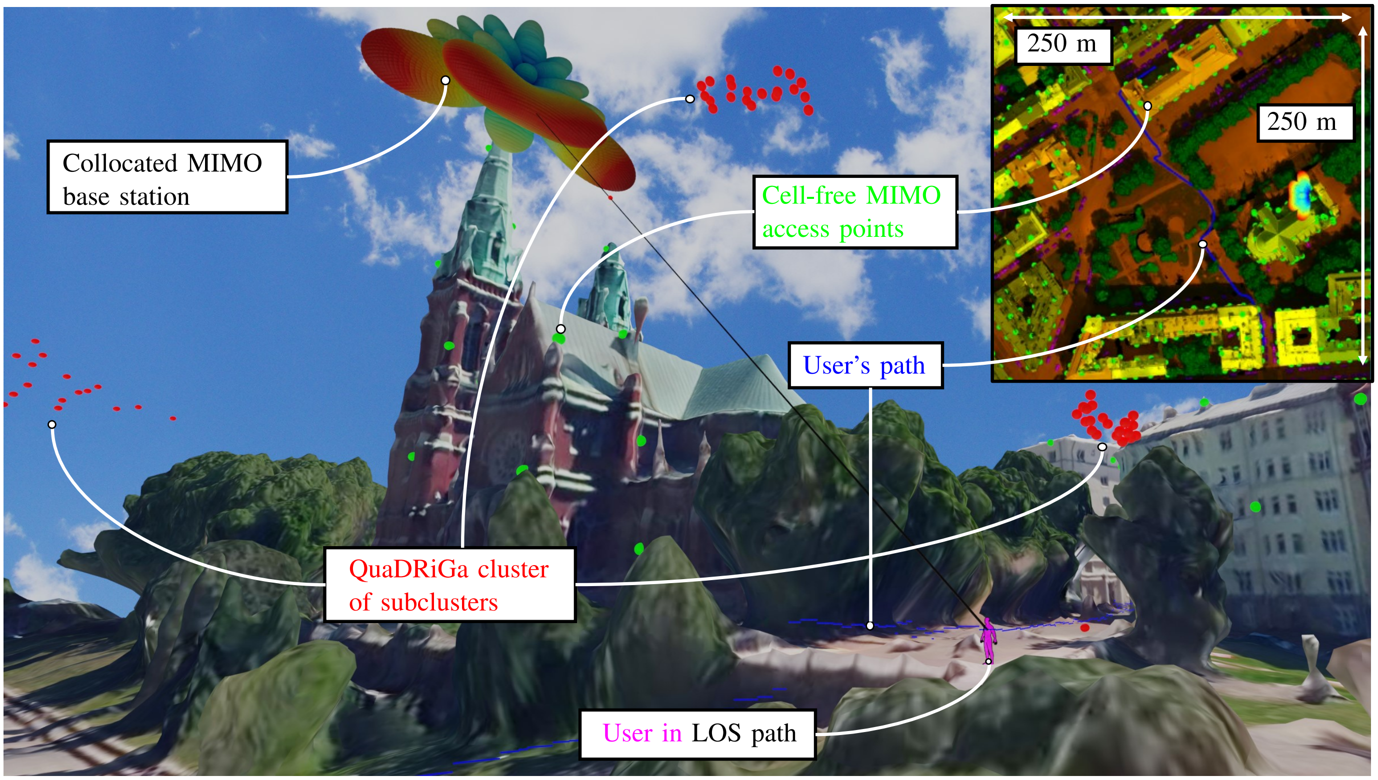

Fig. 5: Configuration of the Helsinki case study. A CF-MaMIMO network (green) is simulated. Alternatively, a collocated MIMO BS beamforms toward the user (purple) at a snapshot in LOS path (black). At this snapshot, the QuaDRiGa clusters, composed of subclusters (red), are shown (acting in free space). The inset depicts the user's path (blue) walking from bottom to top.

$\mathbf{T} = -50\,\mathrm{cm}\,\mathbf{e}_x + 50\,\mathrm{cm}\,\mathbf{e}_z$, with the x-axis in the direction of travel and the z-axis in the vertical direction. This models holding a smartphone in front of the user's torso. Thus, including head-coupling is not necessary as no hot-spot gain is present. Note that the coupling is not necessary in free space when computing S_{inc} due to the experimental assessment procedure of reference quantities [12].

Fig. 6 shows the reference and basic quantities as a function of distance along the path. The exposure is compared for precoded (user scenario) and unprecoded (non-user scenario) transmission, and compared for cell-free and collocated MaMIMO. Colored patches indicate the type of propagation environment along the path of the user. The left axis expresses the exposure for normalized powers per antenna element. This means that the normalized exposure metric $\hat{E}$ is

$$\hat{E} = \frac{E}{N_{\text{AE}}},$$

where E is the exposure metric and N_{AE} equals 64 for the collocated antenna case or 335 for the distributed antenna case. The right axis expresses the ratio to the exposure limits for a typical total power of 320 W. This ratio η therefore equals

$$\eta = P\frac{\hat{E}}{E_{\text{limit}}},$$

where P is the power (320 W) and E_{limit} is the maximum permissible level for the relevant exposure metric. At 28 GHz and for the general public, the reference level is $10\,\mathrm{W/m^2}$ and the basic restriction is $20\,\mathrm{W/m^2}$. The maximum of these ratios is at most 0.05% for a collocated BS precoding the channel in a suburban LOS propagation environment. The range between the minimal and maximal S_{ab} exposure is about 20 dB or 100 times greater with precoded transmission compared to unprecoded transmission, because the beams are steered in the direction of the user. This effect almost completely disappears for CF-MaMIMO, as can be seen in Fig. 6. At any time, only a few APs from different locations serve the user. The precoding gain is determined by the alignment of their phases and amplitudes, making beamforming impossible. The dynamic range of S_{ab} is also 20 dB smaller for the CF-MaMIMO network than for collocated MIMO. This is because the path loss is highest at the start and end of the path. In these urban regions, the user is also in NLOS due to the obstruction of the buildings. The cell-free APN causes a more uniform exposure along the path because, most of the time, at least one AP is in LOS with the user. From a network planning point of view, more power can be fed to a 6G CF-MaMIMO system compared to a 5G collocated one, while avoiding regions of excessive exposure. Furthermore, we observe the continuity (that is, no abrupt jumps) of the channel over time for LSF and report continuity for SSF. Finally, the Pearson correlation coefficients between the exposure quantities (in dB) are shown in Fig. 7. As was also found in [42], the relationship between reference and basic quantities is strong, in this case

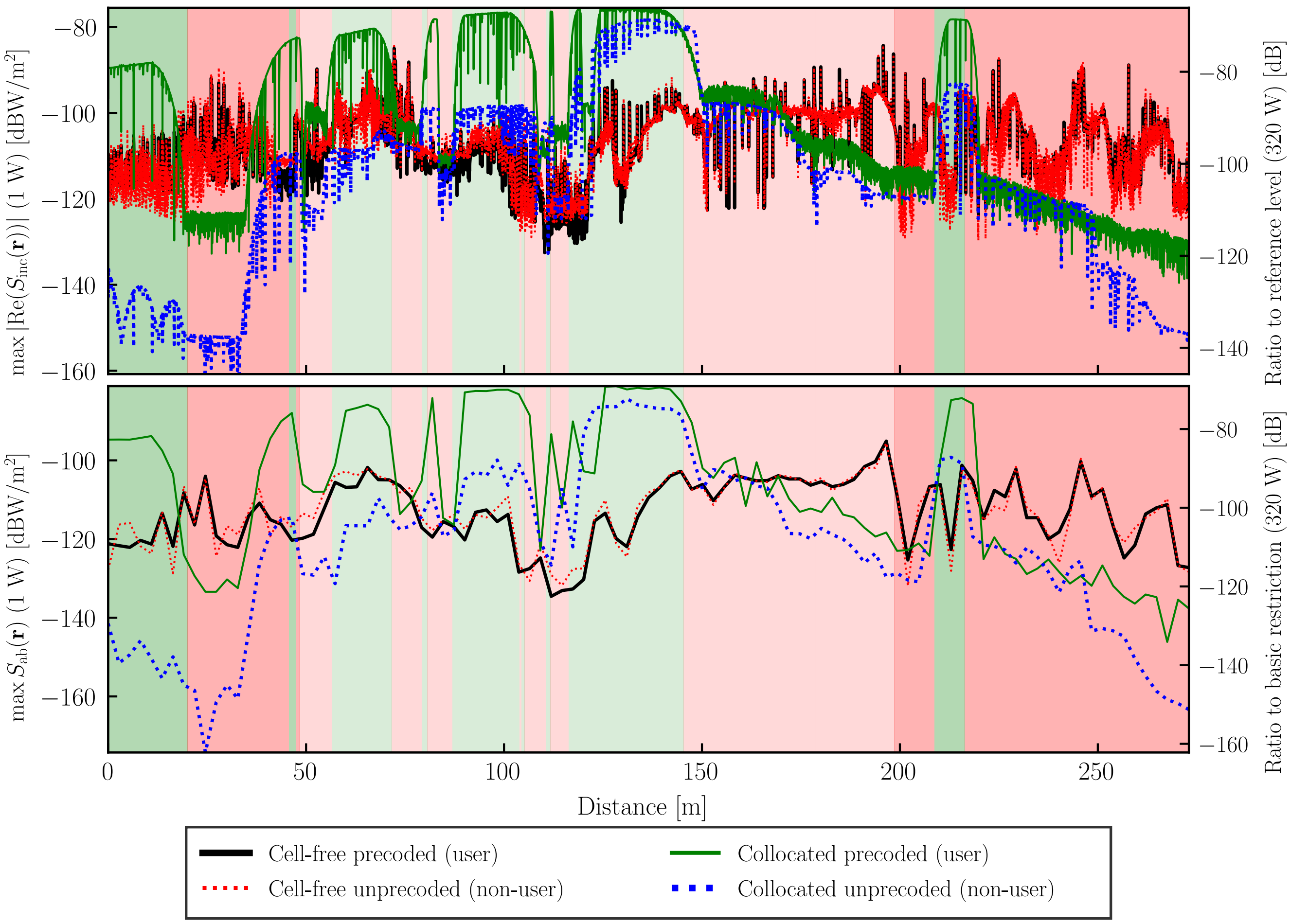

Fig. 6: Reference (top) and basic (bottom) quantities as a function of distance along the path in Helsinki. The exposure is compared for precoded and unprecoded transmission, and compared for cell-free and collocated MaMIMO. Colored patches indicate the type of propagation environment along the path of the user. The left axis expresses the exposure for normalized powers per antenna element. The right axis expresses the exposure as a ratio for a typical total power of 320 W. Green or red patches indicate a LOS or NLOS state with the collocated antenna, respectively. The darker or lighter patches indicate an urban or suburban environment, respectively.

approximately 0.60.

B. *Case study in New York City, USA*

In this case study, RT-based hybrid QuaDRiGa/FDTD is applied to the urban scenario shown in Fig. 1(a). After spending 10 seconds indoors, a smartphone user walks from the One WTC tower southward to Liberty Street in NYC, staying indoors for another 10 seconds. The user passes by an open area with foliage. Cellular APs from neighboring buildings radiate onto the user below the tree cover in either LOS or NLOS. The QuaDRiGa channel model distinguishes and interpolates between these in a continuous fashion. The total duration of the walk is 6 minutes. In this case study, we choose $\mathbf{T} = \mathbf{0}$, corresponding to the user holding a smartphone by the right ear. Thus, including head-coupling is necessary as a hot-spot gain can be present.

The *user/non-user contrast* is defined as the average difference in signal gain between the two users walking 5 meters from each other. The transmit symbol $\boldsymbol{s} = [1\ 0]^T$ is precoded such that the first user is a user and the second user is a non-user. Hence, a high user/non-user contrast shows functioning precoding and the extent of non-user exposure from a large-scale hot-spot created by beamforming. When precoding is applied only on antenna elements within each AP (as in (4)), the user/non-user contrast increases by 6.01 dB along the walk. All APs beamform toward the user, but the closest APs does not necessarily emit most of the power. When precoding is applied only on the APs themselves, the user/non-user contrast increases by 4.74 dB. None of the APs beamform toward the user, but the nearest APs emit most power. When both precodings are combined (equations (4) and (5)), the user/non-user contrast is 10.08 dB.

Fig. 8 shows the exposure metrics S_{inc} and S_{ab} along the walk on the left vertical axis. The maximum S_{inc} is compared with the median S_{inc} in the computational domain to illustrate the hot-spot gain. The precoded transmission case is compared with the unprecoded transmission case. The exposure is constant when the user is indoors. The exposure is continuous in time and consistent with the environment, e.g.,

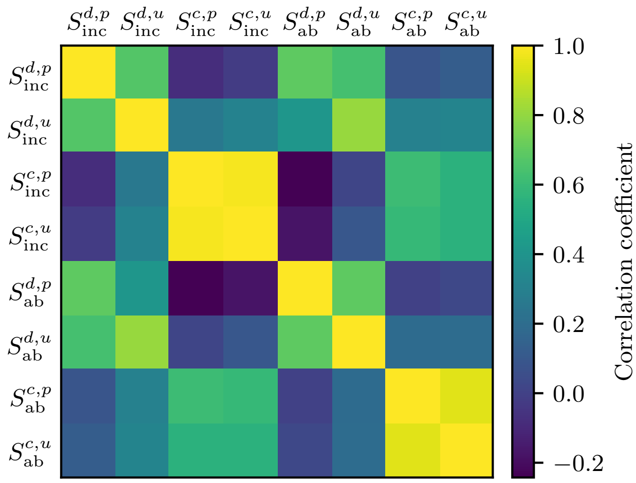

Fig. 7: Correlation matrix between the various exposure metrics shown in Fig. 6, using the Pearson coefficient of the values in dB along the walk. The superscripts c, d, p and u refer to collocated, distributed, precoded and unprecoded, respectively.

TABLE II: A comparison of hot-spot characteristics when defined to be at the receiver or at the point with the highest field near the receiver. The mean and standard deviation are given based on the S_{inc} metric in free space. In this table, d_{center} is the distance of the hot-spot from the center of the evaluation grid (at the UE), P/P ratio is the Peak-to-Prominence ratio of the hot-spot, Dim_3 is the percentage of hot-spots that have a dimensionality of 3.

	At the receiver	**At highest field**
d_{center} [λ]	0.0	2.79 ± 1.12
Peak [nW/m^2]	0.19 ± 0.77	0.41 ± 1.65
FWHM [λ]	1.06 ± 0.41	0.88 ± 0.35
P/P ratio [%]	63 ± 26	57 ± 25
Dim_3 [%]	84.5	96.2

the signal increases substantially when near APs and when the user is in LOS. The maximum exposure metric for S_{inc} and S_{inc} is -78.8 dBW/m^2 and -92.8 dBW/m^2, respectively, for 100 W total power in the CF-MaMIMO network. The ratio of the exposure metric divided by the relevant ICNIRP exposure limit is shown on the right vertical axis.

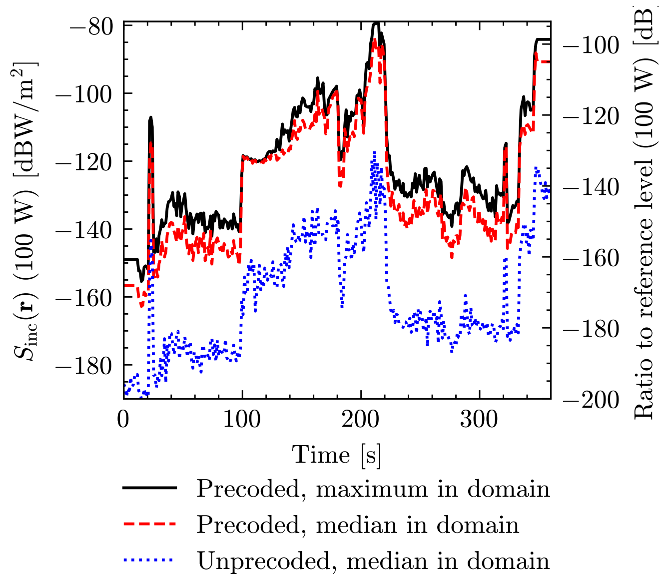

(a) The reference quantity S_{inc} along the path.

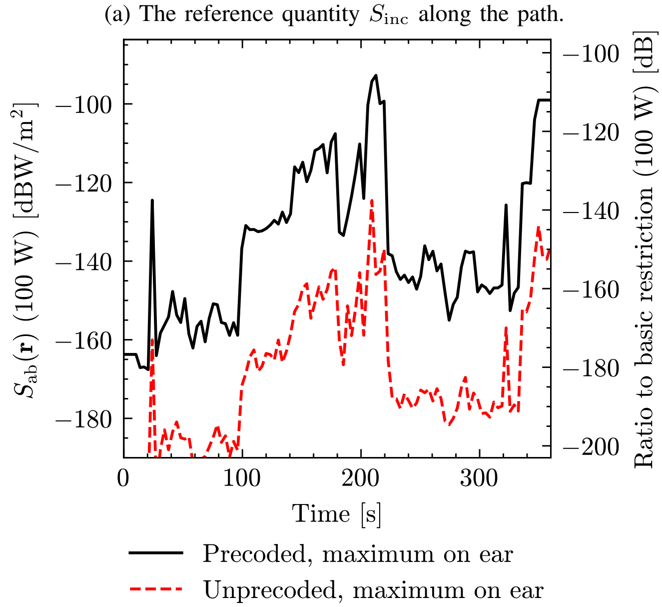

(b) The basic quantity S_{ab} along the path.

Fig. 8: The reference (S_{inc}) and basic (S_{ab}) exposure quantities are plotted along the walk (left vertical axis). The right axis shows the ratio w.r.t. the ICNIRP limits. The influence of the hot-spot is shown in free space.

C. Hot-spots

1) Hot-spot characteristics: Within a large-scale region exposed by the beams, hot-spots can increase the aforementioned 10.08 dB gain locally, at or within several wavelengths of the receiver. A free-space domain of $4.76\lambda \times 3.83\lambda \times 6.63\ \lambda$ (5.1 cm$\times$ 4.1 cm$\times$ 7.1 cm) is considered, fitting a human ear. The mean and standard deviation were computed based on 316 time steps along the walk. These results are shown in Table II.

The means of the FWHM and P/P ratios indicate a size on the order of one wavelength (10.7 mm) and a visible peak, respectively. The distance from the center for the point with the highest field is 2.63 λ on average. However, the number of hot-spots found along the path per λ^3 is highest in the center. More than 50% of the hotspots are within 0.28 λ of the center, with many outliers. As is excepted, the peak expresses high variability because of the log-normal distribution of received signals, as is typical in wireless channels. The standard deviations of the FWHM and P/P ratio are high, approximately 40% of their mean. When examining the field distribution along the walk step by step, the location and shape of the hot-spot changes frequently, but in a continuous fashion due to the time-continuity of the propagation step. During 96% of the walk, the dimensionality is equal to 3, indicating a roughly ellipsoidal or spherical shape. The hot-spots vanish or are reduced to a simple interference pattern when one or two strong LOS components are present, respectively. They also vanish when no precoding is applied.

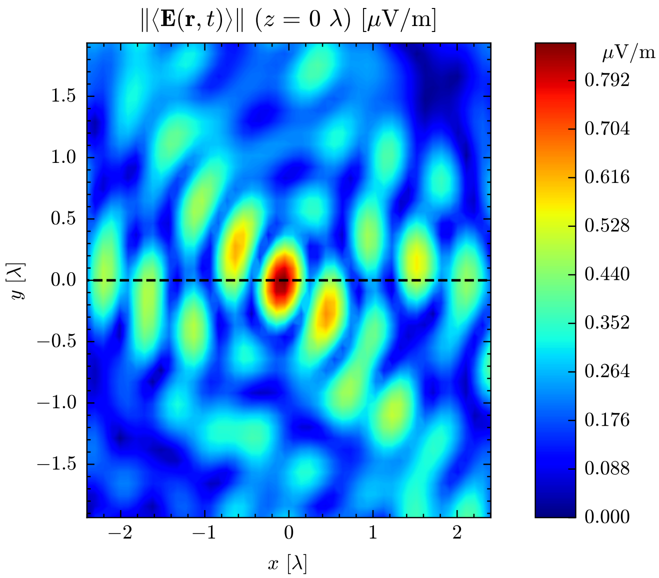

(a) A 2D slice through the focused UE.

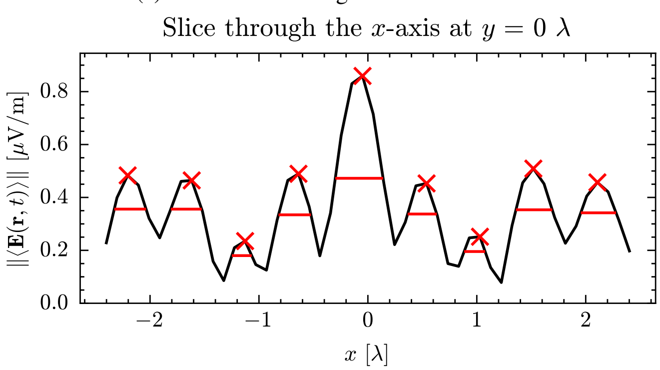

(b) A 1D slice through the focused UE.

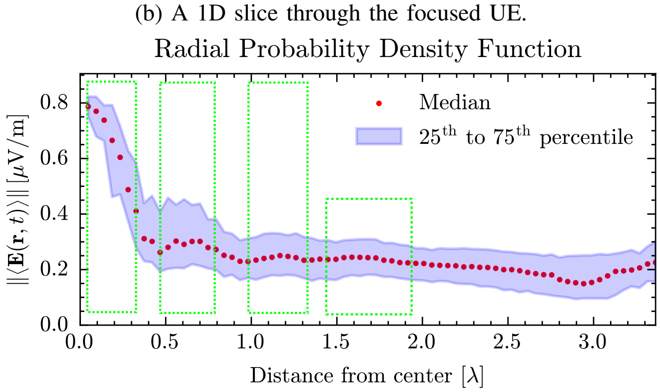

(c) The radial probability density function of the fields, showing the 25^{th}, 50^{th} and 75^{th} percentiles of all fields at distance (± 0.15 mm). The green rectangles indicate the main, first, second, and (faint) third-order sidelobes of the hot-spot.

Fig. 9: Visualization of a hot-spot's electric field when averaged propagation-wise (norm of the time-average).

2) Shape of an average hot-spot: At any specific time step, a hot-spot can appear in a variety of shapes, sizes,

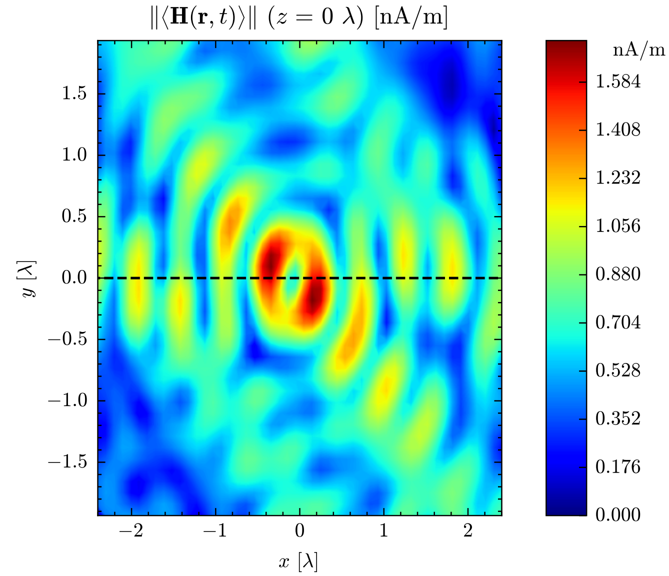

(a) A 2D slice through the focused UE.

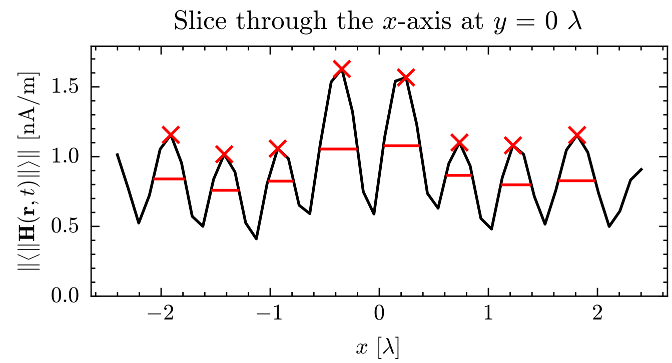

(b) A 1D slice through the focused UE.

Fig. 10: Visualization of a hot-spot's magnetic field when averaged propagation-wise (norm of the time-average).

and locations. However, a characteristic shape appears when the hot-spot is averaged in time. ICNIRP also specifies that exposure metrics should be averaged over 6-minute intervals. Fig. 9(a) depicts a horizontal slice through the receiver, positioned in the center. In a first step, the electric field is examined because its norm features in (10) for propagation-wise S_{inc} and its field is maximized through precoding. The main peak is located in the center with a FWHM of 0.44 λ. The peak is flanked by troughs at 25% of its value, giving a ratio of 75% P/P (90% with the deepest troughs). A first-order sidelobe is observed at 0.61 λ with a peak value equal to 50% of the main peak. A second-order sidelobe is observed at 1.15 λ. Angular dependence is observed in the 2D slice, showing peaks and troughs for certain azimuthal angles. Fig. 9(c) shows the radial probability density function of the field with respect to distance. For a distance $r \pm \mathrm{d}r$ measured from the center of the FDTD domain, the field values are collected in a distribution. The graph displays the 25^{th}, 50^{th} and 75^{th} percentiles of this distribution as a function of r. The same main, first- and second-order sidelobes are observed (shown in green). A faint third-order is observed at 1.76 λ. This is more faint because the peaks and troughs are averaged out in the angular domain. As the distance approaches the edges of the domain, a constant field remains, which is 25% of the peak in the main lobe. Therefore, the small-scale hot-spot increases the electric field by 12 dB on top of the large-scale beamforming gain. A higher number of antenna elements and APs increase this gain, in theory without bounds [52]. Within each sidelobe, peaks and troughs appear as a function of the azimuthal and elevation angles.

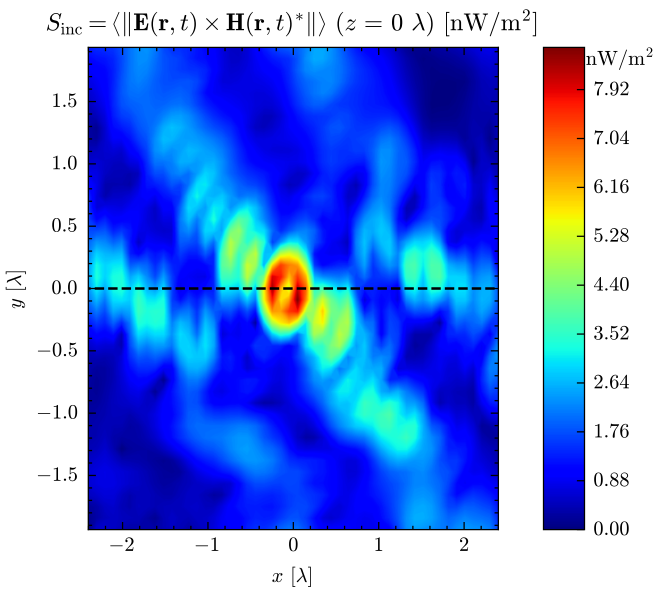

(a) Propagation-wise average of the hot-spot (norm of the time-average).

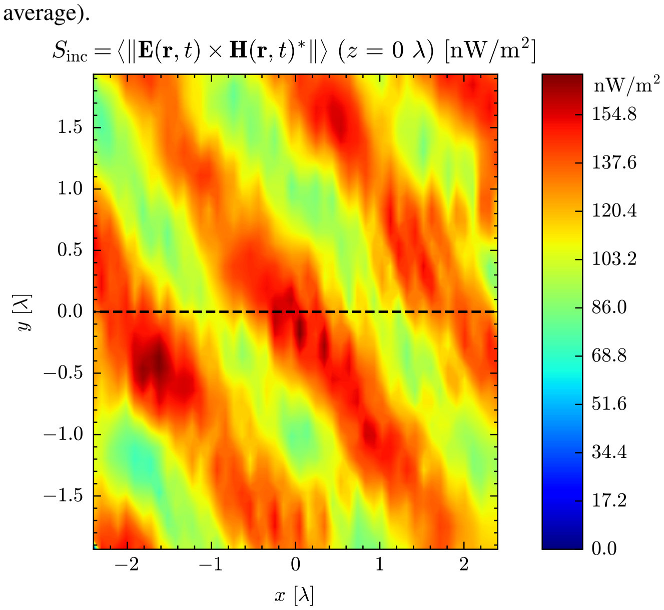

(b) Exposure-wise average of the hot-spot (time-average of the norm).

Fig. 11: Comparison of the S_{inc} with the propagation- and exposure-wise averaging using 2D slices. The former averages the fields in time first, the latter computes the exposure first and then averages these in time.

The magnetic field of the hot-spot behaves analogously to a typical interference pattern: when the electric field reaches a peak in space, the magnetic field reaches a trough, and vice-versa, as can be seen in Fig. 10. Fig. 11(a) shows S_{inc} for the 2D slice. The expression for S_{inc} combines the electric and magnetic fields. The hot-spot also combines the features of the electric and magnetic field hot-spots. The small peak at the center is the combination of an electric-field peak and a magnetic-field trough. This is flanked by higher peaks originating from the first-order magnetic-field sidelobes. The sidelobe series continues with alternating peaks from both fields. This can also be seen in Fig. 12(a)

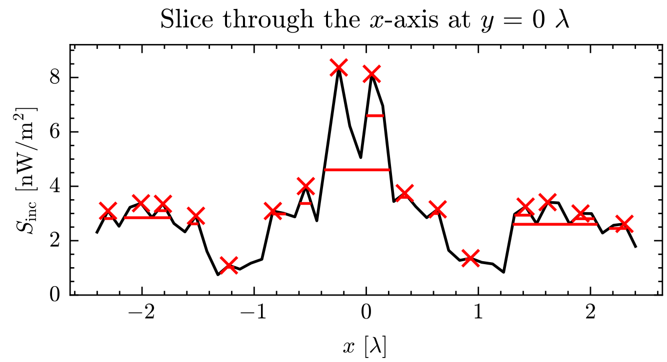

(a) Propagation-wise average of the hot-spot (norm of the time-average).

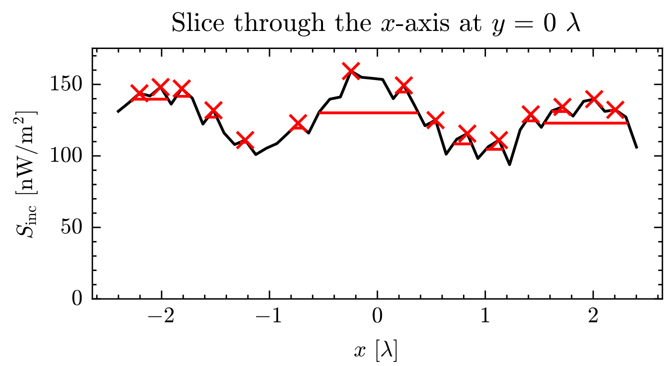

(b) Exposure-wise average of the hot-spot (time-average of the norm).

Fig. 12: Comparison of the S_{inc} with the propagation- and exposure-wise averaging using 1D slices. The slice line is shown as a dashed line in Fig. 11. The former averages the fields in time first, the latter computes the exposure first and then averages these in time.

With propagation-wise averaging, positive EMFs vector components at one time step can cancel out negative EMFs vector components at another time step. However, from an exposure assessment point of view, both positive and negative field values can contribute to dielectric heating. The exposure-wise average of S_{inc} is visualized in Fig. 11(b) in the same 2D slice. A more chaotic interference pattern is seen with its highest peak not at the center. The FWHM is 0.92 λ and the P/P ratio is 37% with the deepest troughs. This can also be seen in Fig. 12(b). The pattern is overlaid on a constant envelope. This causes the first-order troughs to be 2.5 times less deep than with propagation-wise averaging.

IV. Conclusions

This study has presented a comprehensive analysis of human exposure to EMFs in realistic environments using a novel RT-based hybrid QuaDRiGa/FDTD method. By integrating SOTA computational techniques and leveraging high-resolution 3D models from Google Earth, we have demonstrated an efficient and accurate approach to assess exposure in 6G CF-MaMIMO networks operating at 28 GHz.

Key findings from case studies in Helsinki and NYC show the reference and basic exposure metrics along a realistic path, remaining within at most 1% of the ICNIRP guidelines limit. The almost exactly deterministic results indicate that the cell-free MaMIMO system provides a more uniform exposure compared to collocated MaMIMO, with a 20 dB reduction in path loss variability. Furthermore, the detailed hot-spot analysis shows a 12 dB increase in electric field within these localized regions, emphasizing the importance of understanding small-scale exposure variations.

The method enables (1) computing extensive exposure maps anywhere in the world and (2) studying a full digital twin of the entire pipeline, from Tx power control to exposure metric. These offer citizen and policy-makers insight into realistic EMF values, and network planners the ability to model exposure more accurately. Future work should focus on applying the method in different microenvironments and comparing with measurements on city scales. The 12 dB figure is expected to increase when this study is conducted for extremely massive MIMO systems. The method can be further improved with comprehensive data of realistic devices. The Tx and UE antenna patterns as well as their locations and configurations are the intellectual property of private companies. A wide outreach to industry from the scientific community in this field is important for realistic exposure assessment.

V. Acknowledgements

This work was supported in part by the European Research Council (ERC) through ATTO: A New Concept for Ultra-high Capacity Wireless Networks under Grant 695495, in part by Methusalem through SHAPE: Next Generation Wireless Networks, and in part by the Research Foundation Flanders (FWO) through file number K215823N.

References

[1] G. Torfs *et al.*, "ATTO: Wireless Networking at Fiber Speed," *J. of Lightwave Technol.*, vol. 36, no. 8, pp. 1468-1477, Apr. 15, 2018, doi: 10.1109/JLT.2017.2783038.

[2] C.-X. Wang *et al.*, "Cellular architecture and key technologies for 5G wireless communication networks," *IEEE Communications Magazine*, vol. 52, no. 2, pp. 122-130, Feb. 2014, doi: 10.1109/MCOM.2014.6736752.

[3] "Advanced 5G with Millimeter Wave Penetration, Version 1.0," 5th Generation Mobile Communications Promotion Forum, March 2024. [Online]. Available: https://www.telegraphic.jp/en/2023/12/107/. [Accessed: Oct. 2024].

[4] T. L. Marzetta, "Noncooperative Cellular Wireless with Unlimited Numbers of Base Station Antennas," *IEEE Trans. on Wireless Commun.*, vol. 9, no. 11, pp. 3590-3600, Nov. 2010, doi: 10.1109/TWC.2010.092810.091092.

[5] Y. Niu, Y. Li, D. Jin, L. Su, A. V. Vasilakos, "A survey of millimeter wave communications (mmWave) for 5G: opportunities and challenges," *Wireless Networks*, vol. 21, pp. 2657–2676, 2015, doi: 10.1007/s11276-015-0942-z.

[6] X. You, D. Want and J. Wang, *Distributed MIMO and Cell-Free Mobile Communication*, 1st ed. Singapore: Springer and Science Press, 2021.

[7] H. Q. Ngo, A. Ashikhmin, H. Yang, E. G. Larsson, and T. L. Marzetta, "Cell-free massive MIMO: Uniformly great service for everyone," in *Proc. 16th IEEE Int. Workshop Signal Process. Adv. Wireless Commun.*, Stockholm, Sweden, Jun. 2015, pp. 201-205, doi: 10.1109/SPAWC.2015.7227028.

[8] H. Q. Ngo, A. Ashikhmin, H. Yang, E. G. Larsson and T. L. Marzetta, "Cell-Free Massive MIMO Versus Small Cells," *IEEE Trans. Wirel. Commun.*, vol. 16, no. 3, pp. 1834-1850, March 2017, doi: 10.1109/TWC.2017.2655515.

[9] Z. H. Shaik, E. Björnson, and E. G. Larsson, "Cell-Free Massive MIMO with Radio Stripes and Sequential Uplink Processing," *Proc. IEEE Int. Conf. Commun. Workshops (ICC Workshops)*, Dublin, Ireland, 2020, pp. 1-6, doi: 10.1109/ICCWorkshops49005.2020.9145164.

[10] L. Chiaraviglio, A. Elzanaty, and M. -S. Alouini, "Health Risks Associated With 5G Exposure: A View From the Communications Engineering Perspective," *IEEE Open J. Commun. Soc.*, vol. 2, pp. 2131-2179, 2021, doi: 10.1109/OJCOMS.2021.3106052.

[11] M. Farhan and M. Y. Osman, "Concerns over 5G Mobile Networking Technology," *Scientific Writing and Communication*, University of Malaya, June 2020. [Online]. Available: https://www.researchgate.net/publication/342512892_Concerns_over_5G_Mobile_Networking_Technology. [Accessed: Oct. 2024].

[12] International Commission on Non-Ionizing Radiation Protection, "Guidelines for limiting exposure to electromagnetic fields (100 KHz to 300 GHz)," *Health Phys.*, vol. 118, no. 5, pp. 483–524, 2020, doi: 10.1097/HP.0000000000001210.

[13] A. Hirata et al., "Assessment of Human Exposure to Electromagnetic Fields: Review and Future Directions," *IEEE Trans. Electromagn. Compat.*, vol. 63, no. 5, pp. 1619-1630, Oct. 2021, doi: 10.1109/TEMC.2021.3109249.

[14] S. Shikhantsov, A. Thielens, G. Vermeeren, P. Demeester, L. Martens, and W. Joseph, "Numerical Assessment of Human EMF Exposure to Collocated and Distributed Massive MIMO Deployments in an Industrial Indoor Environment," *IEEE Trans. Electromagn. Compat.*, vol. 65, no. 4, pp. 960-971, Aug. 2023, doi: 10.1109/TEMC.2023.3273475.

[15] R. Wydaeghe *et al.*, "New Hybrid Ray-Tracing/FDTD for EMF Exposure in 6G Networks using Semantically Classified Google Earth Photogrammetry with Measurement Validation," *18th Eur. Conf. on Ant. and Prop.*, Glasgow, Scotland, Mar. 2024.

[16] R. Wydaeghe, S. Shikhantsov, E. Tanghe, G. Vermeeren, W. Joseph, "Characterization of EMF hotspots for realistic exposure assessment in end-to-end simulations using a hybrid QuaDRiGa/FDTD tool," *3rd Int. Conf. Bioelectromagnetics*, Crete, Greece, Jun. 2024.

[17] E. Björnson, J. Hoydis and L. Sanguinetti, "Introduction and Motivation," in Massive MIMO Networks: Spectral, Energy, and Hardware Efficiency, *USA: Found. Trends Signal Process.*, 2017, ch. 1, p. 204, doi: 10.1561/2000000093.

[18] Google, "Photorealistic 3D Tiles — Google Maps Tile API," [Online]. Available: https://developers.google.com/maps/documentation/tile/3d-tiles. [Accessed: Oct. 2024].

[19] D. He, G. Liang, J. Portilla and T. Riesgo, "A novel method for radio propagation simulation based on automatic 3D environment reconstruction," *6th Eur. Conf. on Ant. and Prop.*, Prague, Czech Republic, 2012, pp. 1445-1449, doi: 10.1109/EuCAP.2012.6206457.

[20] D. He, B. Ai, K. Guan, L. Wang, Z. Zhong, and T. Kürner, "The Design and Applications of High-Performance Ray-Tracing Simulation Platform for 5G and Beyond Wireless Communications: A Tutorial," *IEEE Communications Surveys & Tutorials*, vol. 21, no. 1, pp. 10-22, 2019, 10.1109/COMST.2018.2865724.

[21] W. Gao, L. Nan, B. Boom, and H. Ledoux, "SUM: A benchmark dataset of Semantic Urban Meshes," *ISPRS J. Photogramm. Remote Sens.*, vol. 179, pp. 108-120, 2021, doi: 10.1016/j.isprsjprs.2021.07.008.

[22] S. Shikhantsov *et al.*, "Hybrid Ray-Tracing/FDTD Method for Human Exposure Evaluation of a Massive MIMO Technology in an Industrial Indoor Environment," *IEEE Access*, vol. 7, pp. 21020-21031, Feb. 2019, doi: 10.1109/ACCESS.2019.2897921.

[23] A. W. Mbugua *et al.*, "Review on Ray Tracing Channel Simulation Accuracy in Sub-6 GHz Outdoor Deployment Scenarios," *IEEE Open J. Antennas Propag.*, vol. 2, pp. 22-33, Jan. 2021, doi: 10.1109/OJAP.2020.3041953.
[24] R. Wydaeghe *et al.*, "New Hybrid QuaDRiGa-FDTD Method for Realistic Human Exposure Assessment at 28 GHz with 6G Cell-Free Massive MIMO in 3D Outdoor Environments," *2nd Int. Conf. Bioelectromagnetics*. presented at BioEM 2023, Oxford, United Kingdom, June 18-23, 2023.
[25] S. Jaeckel, L. Raschkowski, K. Börner, and L. Thiele, "QuaDRiGa: A 3-D Multi-Cell Channel Model With Time Evolution for Enabling Virtual Field Trials," *IEEE Trans. Antennas Propag.*, vol. 62, no. 6, pp. 3242-3256, June 2014, doi: 10.1109/TAP.2014.2310220.
[26] R. Heijs, G. Steinböck, B. -E. Olsson, M. Johansson, and B. Smolders, "On the Importance of Scattering from Poles in Ray Tracing Simulations," *18th Eur. Conf. on Ant. and Prop.*, Glasgow, United Kingdom, 2024, pp. 1-5, doi: 10.23919/EuCAP60739.2024.10501579.
[27] F. Bianconi, M. Filippucci, F. Cornacchini, and A. Migliosi, "The impact of Google's APIs on landscape virtual representation," *Int. Arch. Photogramm. Remote Sens. Spatial Inf. Sci.*, vol. XLVIII-4/W9-2024, pp. 91–98, 2024, doi: 10.5194/isprs-archives-XLVIII-4-W9-2024-91-2024.
[28] Google Earth, 2024. World Trade Center, New York City. Google Earth [online]. Available: https://earth.google.com/web/@40.71200981,-74.0127844,4.66348666a,537.65188487d,35y,38.88984458h,43.8020311t,-0r. [Accessed Oct. 2024].
[29] Google, "Google Maps Directions API," Google Developers. [Online]. Available: https://developers.google.com/maps/documentation/directions/overview. [Accessed: Oct. 2024].
[30] OpenCelliD, "The world's largest Open Database of Cell Towers," OpenCelliD.org. [Online]. Available: https://www.opencellid.org/. [Accessed: Oct. 2024].
[31] R. Bridson, "Fast Poisson disk sampling in arbitrary dimensions," *ACM SIGGRAPH 2007 Sketches*, San Diego, California, USA, 2007, pp. 22–es. doi: 10.1145/1278780.1278807.
[32] C.-X. Wang, J. Bian, J. Sun, W. Zhang, and M. Zhang, "A Survey of 5G Channel Measurements and Models," *IEEE Commun. Surv. & Tutor.*, vol. 20, no. 4, pp. 3142-3168, Fourth Quarter 2018, doi: 10.1109/COMST.2018.2862141.
[33] K. H. Ng, E. K. Tameh, A. Doufexi, M. Hunukumbure and A. R. Nix, "Efficient Multielement Ray Tracing With Site-Specific Comparisons Using Measured MIMO Channel Data," *IEEE Trans. Veh. Technol.*, vol. 56, no. 3, pp. 1019-1032, May 2007, doi: 10.1109/TVT.2007.895606.
[34] Remcom, "Wireless InSite," [Software]. Available: https://www.remcom.com/wireless-insite-em-propagation-software. [Accessed: Oct. 2024].
[35] International Telecommunications Union Radiocommunication Sector, "Effects of Building Materials and Structures on Radiowave Propagation Above About 100MHz," Recommendation P.2040, ITU-R, approved August 23, 2023. [Online]. Available: https://www.itu.int/rec/R-REC-P.2040/en. [Accessed: Oct., 2024].
[36] S. Shikhantsov *et al.*, "Ray-Tracing-Based Numerical Assessment of the Spatiotemporal Duty Cycle of 5G Massive MIMO in an Outdoor Urban Environment," *Appl. Sci.*, vol. 10, no. 21, p. 7631, Oct. 2020, doi: 10.3390/app10217631.
[37] S. Jaeckel, "Quasi-Deterministic Channel Modeling and Experimental Validation in Cooperative and Massive MIMO Deployment Topologies," Ph.D. dissertation, Dept. Electrotech. and Infotech., Techn. Univ. Ilmenau, Ilmenau, Germany, 2017.
[38] S. Jaeckel *et al.*, "Industrial Indoor Measurements from 2-6 GHz for the 3GPP-NR and QuaDRiGa Channel Model," *Proc. IEEE 90th Veh. Technol. Conf. (VTC-Fall)*, Honolulu, HI, USA, 2019, pp. 1-7, doi: 10.1109/VTCFall.2019.8891356.
[39] S. Dai, N. Abdellatif, M. Kurras, S. Jaeckel and L. Thiele, "Spatial Consistency Validation on Massive SIMO Covariance Matrices in the Geometry-Based Stochastic Channel Model QuaDRiGa," WSA 2020; 24th International ITG Workshop on Smart Antennas, Hamburg, Germany, 2020, pp. 1-6.
[40] S. Jaeckel, L. Raschkowski, and L. Thiele, "QuaDRiGa - Quasi Deterministic Radio Channel Generator, User Manual and Documentation," Fraunhofer Heinrich Hertz Inst., Tech. Rep. v2.6.1, 2021.
[41] H2020-ICT-671650-mmMAGIC/D2.2, "mmMAGIC D2.2 - measurement results and final mmMAGIC channel models," Tech. Rep., 2017.
[42] R. Wydaeghe *et al.*, "Realistic human exposure at 3.5 GHz and 28 GHz for distributed and collocated MaMIMO in indoor environments using hybrid ray-tracing and FDTD," *IEEE Access*, vol. 10, pp. 130996-131004, 2022, doi: 10.1109/ACCESS.2022.3227107.
[43] D. He, B. Ai, K. Guan, Z. Zhong, L. Tian, and J. Dou, "Ray-tracing Assisted 3GPP Stochastic Channel Modeling for High-speed Railway Rural Scenario," *2nd URSI AT-RASC*, Gran Canaria, Spain, 28 May – 1 June 2018.
[44] C. Lee, C. -B. Chae, T. Kim, S. Choi and J. Lee, "Network massive MIMO for cell-boundary users: From a precoding normalization perspective," 2012 IEEE Globecom Workshops, Anaheim, CA, USA, 2012, pp. 233-237, doi: 10.1109/GLOCOMW.2012.6477575.
[45] P. Bernardi, M. Cavagnaro, S. Pisa and E. Piuzzi, "Human exposure to radio base-station antennas in urban environment," *IEEE Trans. Microw. Theory Techn.*, vol. 48, no. 11, pp. 1996-2002, Nov. 2000, doi: 10.1109/22.884188.
[46] S. Shikhantsov *et al.*, "Massive MIMO Propagation Modeling With User-Induced Coupling Effects Using Ray-Tracing and FDTD," *IEEE J. Sel. Areas Commun.*, vol. 38, no. 9, pp. 1955-1963, Sept. 2020, doi: 10.1109/JSAC.2020.3000874.
[47] C. A. Balanis, *Antenna Theory: Analysis and Design*, 4th ed. Hoboken, NJ, USA: Wiley, 2016.
[48] M. I. Iacono et al., "MIDA: A Multimodal Imaging-Based Detailed Anatomical Model of the Human Head and Neck," Public Library of Science, vol. 10, no. 4, pp. 1-35, 2015, 10.1371/journal.pone.0124126.
[49] A. Christ, A. Aeschbacher, F. Rouholahnejad, T. Samaras, B. Tarigan, and N. Kuster, "Reflection Properties of the Human Skin From 40 to 110GHz: A Confirmation Study." Bioelectromagnetics, 42: 562-574, Jul. 2021, doi: 10.1002/bem.22362.
[50] *Sim4Life Application and Support Team*, *Sim4Life Reference Guide*, Release 7.2, Zurich, Switzerland: ZMT Zurich MedTech AG, Dec. 2022.
[51] IEC/IEEE International Standard - Assessment of power density of human exposure to radio frequency fields from wireless devices in close proximity to the head and body (frequency range of 6 GHz to 300 GHz)–Part 2: Computational procedure, IEEE/IEC 63195-2-2022, May 2022.
[52] G. J. Foschini and M. J. Gans, "On Limits of Wireless Communications in a Fading Environment when Using Multiple Antennas," *Wireless Personal Communications*, vol. 6, no. 3, pp. 311-335, 1998, doi: 10.1023/A:1008889222784.

Robin Wydaeghe received the B.Sc and M.Sc degrees in engineering physics from Ghent University, Ghent, Belgium, in 2019 and 2021, respectively. He is currently pursuing the Ph.D. degree in engineering physics with IMEC and Ghent University. His research interests include computational electrodynamics, numerical assessment of human electromagnetic field exposure, and propagation modeling of next generation wireless networks.

Sergei Shikhantsov received the M.Sc. degree in applied physics and mathematics from the Moscow Institute of Physics and Technology (MIPT), Moscow, Russia, in 2016. He received the Ph.D. degree in engineering physics from Ghent University, Ghent, Belgium, in 2022. He is currently working as a Post-Doctoral Researcher at Ghent University.

Emmeric Tanghe was born in Tielt, Belgium, in 1982. He received the M.Sc. and Ph.D. degrees in electrical engineering from Ghent University, Ghent, Belgium, in 2005 and 2011, respectively. From 2005 to 2011, he was a Research Assistant with the Department of Information Technology, Ghent University-imec. His scientific research focused on the modeling of indoor and outdoor propagation through field measurements. In 2015, he became a Part-Time Professor in medical applications of electromagnetic fields in and around the human body. Since 2011, he has been a Postdoctoral Researcher with Ghent University-imec, where he focuses on propagation modeling. From 2012 to 2018, he was a Postdoctoral Fellow of FWO-V (Research Foundation-Flanders).

Günter Vermeeren received the M.Sc. degree in industrial engineering from the KAHO Sint-Lieven, Ghent, Belgium, in July 1998, and the M.Sc. degree in electrical engineering and the Ph.D. degree in electro-technical engineering from Ghent University, Belgium, in July 2001 and August 2013, respectively. From September 2001 to September 2002, he was with the Research and Development Department of network integrator Telindus, Leuven, Belgium. Since September 2002, he has been a Research Engineer with the WiCa group in the Department of Information Technology at Ghent University. His research interests include the numerical modeling as well as measurements of electromagnetic radiation in the domain of radio-frequency dosimetry, electromagnetic exposure, on-body propagation, interference in communication networks, and medical imaging systems, such as, hybrid MRI systems.

Luc Martens received the M.Sc. degree in electrical engineering from Ghent University, Ghent, Belgium, in 1986, and the Ph.D. degree in 1990. From September 1986 to December 1990, he was a Research Assistant with the Department of Information Technology (INTEC), Ghent University. During this period, his scientific work focused on the physical aspects of hyperthermic cancer therapy. His research work dealt with electromagnetic and thermal modeling, and the development of measurement systems for that application. Since 1991, he manages the WAVES research group (at the time; the Wireless and Cable Research Group), INTEC. This group is part of IMEC Institute since 2004. Since April 1993, he has been a Professor with Ghent University. He has authored/coauthored more than 300 publications in the domain of electromagnetic channel predictions, dosimetry, exposure systems and health, and wireless communications. His research interests include modeling and measurement of electromagnetic fields around base stations for mobile communications, health effects of exposure to electromagnetic radiation, electromagnetic exposure assessment, propagation for wireless communication systems, and antennas and calibration. Furthermore, he specializes in wireless performance analysis and quality of experience.

Piet Demeester is currently a Professor with Ghent University–imec, Ghent, Belgium, where he is also the Department Director of the IDLab. He has coauthored over 1000 international publications. His research interests include distributed intelligence in the Internet of Things, machine learning and data mining, semantic intelligence, cloud and big data infrastructures, fixed networking, wireless networking, electromagnetics, and high-frequency design. He received the advanced ERC Grant.

Wout Joseph was born in Ostend, Belgium, in October 1977. He received the M.Sc. degree in electrical engineering from Ghent University, Ghent, Belgium, in 2000, and the Ph.D. degree in electrical engineering, Ghent University, Ghent, in 2005. From September 2000 to March 2005, he was a Research Assistant with the Department of Information Technology (INTEC), Ghent University. During this period, his scientific work focused on electromagnetic exposure assessment. Since April 2005, he has been a Post-Doctoral Researcher with imec-UGent/INTEC. From October 2007 to October 2013, he was a Post-Doctoral Fellow of FWO-V (Research Foundation-Flanders). Since October 2009, he has been a Professor in the domain of experimental characterization of wireless communication systems. His research interests include measuring and modeling electromagnetic fields around base stations for mobile communications, health effects of exposure to electromagnetic radiation, electromagnetic exposure assessment, propagation for wireless communication systems, and antennas and calibration. Furthermore, he specializes in wireless performance analysis and quality of experience.